Analysis of real-fluid thermodynamic effects on turbulent statistics in transcritical channel flows

Fangbo Li,[1] Jack Guo,[2] Bofeng Bai,[1] and Matthias Ihme[2]
[1]*State Key Laboratory of Multiphase Flow in Power Engineering, Xi'an Jiaotong University, Xi'an, Shaanxi 710049, China*
[2]*Department of Mechanical Engineering, Stanford University, Stanford, California 94305, USA*

(Received 9 August 2022; accepted 12 January 2023; published 13 February 2023)

Wall-bounded turbulence at high-pressure transcritical conditions with intense density fluctuations are encountered in many technical applications. In this study, we analyze the turbulent energy transport in transcritical channel flows specifically focusing on dissipation rate, turbulent kinetic energy budgets, heat fluxes, and momentum-fluctuation statistics; results from this analysis are used to guide the development of turbulent scaling laws. We find that the dissipation rate of turbulent kinetic energy is dominated by the enstrophy in the logarithmic layer, and the fluctuating viscosity results in the reduced tilting of the vortical structures and the attenuation of streamwise vorticity in the near-wall layer; the fluctuating viscosity attenuates the dissipation rate by reducing the shear strain and the enstrophy production. Local equilibrium of the turbulent kinetic energy exists in the logarithmic layer. We show that the real-fluid thermodynamic effects significantly change the turbulent heat flux correlated with the sweep and the ejection events; the density changes alter the turbulent transport and result in noticeable magnitudes of density-fluctuation-related momentum-fluctuation statistics. From these results, scaling laws for the turbulent length scales and turbulent kinetic energy budgets are proposed, thereby contributing to improvement of the wall models in large-eddy simulations and Reynolds-averaged Navier-Stokes (RANS) simulations.

DOI: 10.1103/PhysRevFluids.8.024605

I. INTRODUCTION

The thermodynamic properties of fluids at supercritical pressures differ from those at subcritical conditions. At these conditions, the interface between the liquidlike and vaporlike phases disappears into a continuous transition [1,2]. Due to real-fluid effects, thermophysical properties, including density, specific heat capacity, viscosity, and thermal conductivity, vary significantly across the Widom line, which demarcates the state of maximum constant-pressure specific heat at a given pressure [1,3]. Variations in density and viscous-diffusive properties result in substantially modified turbulence statistics and structural behavior when compared to wall-bounded flows at atmospheric pressures. The physical understanding of turbulence and heat transfer of wall-bounded flows at these conditions is crucial for developing reliable computational models.

The existing knowledge of turbulent heat transfer at transcritical conditions mainly comes from direct numerical simulations (DNSs) [4–7]. Bae *et al.* [8] conducted DNSs of pipe flows with uniform wall heat flux to examine the turbulent kinetic energy and its production. The study found that the Morkovin's hypothesis [9] is invalid. Past studies have also found that the heat transfer at supercritical pressures depends on both the ejection as well the sweep motions [10]; the large variations in thermal properties at supercritical pressure were found to have a pronounced effect on these coherent motions. Peeters *et al.* [5] found that the thermal expansion tends to decrease

the coherence of the streaks. DNSs of transcritical channel flows by Kim *et al.* [6] showed that the probability density functions (PDFs) of density and temperature fluctuations at transcritical conditions exhibit a substantially narrower distribution and pronounced kurtosis compared with statistics at subcritical conditions. Significant skewness of density fluctuations was observed in the buffer layer, which is explained by intermittent events resulting from the energy transfer between the liquidlike layer and the vaporlike layer [6]. Li *et al.* [11] uncovered the mechanism of the failure of semilocal scaling from the viewpoint of near-wall structures, and provided a theoretical basis for the scaling law of velocity fluctuations by characterizing the attached eddies. Despite the differences from subcritical pressure flows, a quadrant analysis [4] confirmed that the near-wall density fluctuations have an insignificant effect on turbulent heat fluxes and their transport.

Commonly, studies of transcritical flows and variable-property flows have been limited to a relatively small and moderate density ratio Ω, of $O(1)$. Here, we define the density ratio Ω in channel flows as $\Omega = \rho_c/\rho_h$, with ρ_c being the cold wall density and ρ_h being the hot wall density. There have been limited efforts made to understand the conditions in realistic applications that involve Ω of $O(10–100)$. Ma *et al.* [12] reported turbulent structures in channel flow DNSs with $\Omega = 18$, showing that the velocity structure function follows a logarithmic scaling and the streamwise energy spectrum exhibits an inverse wave-number scaling, providing support to the attached-eddy model at transcritical conditions. Kawai [13] conducted DNSs on a transcritical flat-plate turbulent boundary layer in which the mean density varies by a factor of 20 from the wall to the free stream. It was found that the abrupt density fluctuations induce a turbulent mass flux which not only increases the Favre-averaged velocity fluctuations in the low-speed streaks related to ejection but also reduces velocity fluctuations in the high-speed streaks related to sweep. High density ratios result in different statistical behaviors compared to cases with a smaller density difference. Although many efforts have been conducted to characterize turbulent boundary layers in transcritical wall-bounded flows, several questions remain. Towards improving our understanding of transcritical flows, the following issues need be identified:

(i) Examining effects of the real-fluid thermodynamic properties on turbulent energy transport, including turbulent kinetic energy, dissipation rate, heat fluxes, and momentum-fluctuation moments in transcritical wall-bounded flows: the evolution of these quantities should be addressed for improving the scalings of velocity and thermal statistics [14–17].

(ii) Developing scaling laws for transcritical wall-bounded flows: given the strong fluctuating density, previous scaling laws that attempt to predict the near-wall profiles [12,18–22] should be examined to guide the development of improved wall models in Wall-Modeled Large Eddy Simulation (WMLES) and RANS.

To address these two issues, we analyze DNS data of transcritical channel flows of nitrogen with Ω up to 18 and examine the budgets of dissipation rate, turbulent kinetic energy, and momentum-fluctuation statistics. We also examine the transport of turbulent heat flux in relevance towards predicting heat transfer in transcritical flows. Using these results, scaling laws of turbulent length scales and TKE budget terms are proposed. Our goal is to extend these findings to develop physical models that more closely simulate realistic conditions in modern engineering systems of transcritical turbulent flows.

The remainder of this paper is organized as follows. Section II introduces our DNS methodology for transcritical flows. Section III presents the results and discussions, and concluding remarks are given in Sec. IV.

II. COMPUTATIONAL SETUP

In this study, DNS data of a channel flow are analyzed. The working fluid is nitrogen, which has a critical pressure of $p_c = 3.3958$ MPa and a critical temperature of $T_c = 126.19$ K. The temperatures for the hot wall and the cold wall are kept spatially and temporally constant. The flow domain is of size L_x (streamwise) $\times 2L_y$ (wall normal) $\times L_z$ (spanwise), with $L_x/L_y = 2\pi$, $L_z/L_y = 4\pi/3$, and with channel half-height being $L_y = 0.045$ mm. The flow has a bulk pressure of $p_b = 3.87$ MPa

TABLE I. Summary of cases and conditions, with the subscripts *hot* and *cold* indicating the values at the hot wall and the cold wall.

Cases	$T_{r,\,\mathrm{hot}}$	$T_{r,}$cold	$\rho_{r,}$ hot	$\rho_{r,}$ cold	$\mathrm{Re}_{\tau,}$ hot	$\mathrm{Re}_{\tau,}$ cold	Ω
TR1	0.79	0.79	2.17	2.17	300	300	1
TR1.4	1.11	0.79	0.42	2.17	1370	500	5.2
TR1.9	1.51	0.79	0.22	2.17	610	440	10
TR3	2.38	0.79	0.12	2.17	300	430	18

(corresponding to a reduced pressure of $p_r = 1.14$) and is driven by a streamwise body force so that the mass flow rate is kept constant. The streamwise, wall-normal, and spanwise coordinates are defined over the ranges $0 \leqslant x \leqslant L_x$, $-L_y \leqslant y \leqslant L_y$, and $0 \leqslant z \leqslant L_z$, respectively.

We use the Peng-Robinson (PR) equation [12,22] as the equation of state (EoS):

$$p = \frac{\rho RT}{1 - b\rho} - \frac{\rho^2 a}{1 + 2b\rho - b^2\rho^2}, \tag{1}$$

where R is the gas constant and the parameters a and b accounting for real-fluid effects are given as

$$a = 0.457\,236 \frac{R^2 T_c^2}{p_c}\left[1 + c\left(1 - \sqrt{\frac{T}{T_c}}\right)\right]^2, \tag{2}$$

$$b = 0.077\,796 \frac{R^2 T_c}{p_c}, \tag{3}$$

with

$$c = 0.374\,64 + 1.542\,26\omega - 0.269\,92\omega^2, \tag{4}$$

and with ω being the acentric factor. For N_2, $b = 8.58 \times 10^{-4}$ and $c = 0.432$. The transport properties (viscosity μ and thermal conductivity λ) are evaluated by Chung's model for high-pressure fluids [23–25]. These models for thermal properties have been employed and examined in our previous works [12,22].

We present results for four cases, TR3, TR1.9, TR1.4, and TR1, as summarized in Table I. Cases TR3, TR1.9, and TR1.4 are transcritical with a reduced temperature of $T_{r,\,\mathrm{cold}} = 0.79$ at the cold wall. In case TR1, the two reduced wall temperatures are the same at 0.79, resulting in a constant-property flow with negligible conductive wall heat transfer. For all cases, the domain is discretized using a structured grid with mesh size $N_x \times N_y \times N_z = 384 \times 256 \times 384$, with the spatial resolutions shown in Table II in Appendix B. After the flow reaches a statistically steady state, we average over homogeneous directions and time using more than ten flow-through times to obtain statistically converged results; one flow-through time is defined as $L_x/\overline{u_b}$ with $\overline{u_b}$ being the bulk velocity. Further details on the DNS configurations, methodology, validations, and mesh convergence analysis can be found in Ma *et al.* [12] and Guo *et al.* [22].

III. RESULTS AND DISCUSSION

In this section, DNS results of turbulent energy transport are presented. We denote the Reynolds average of a variable ϕ as $\bar{\phi}$, and the Favre average quantity is defined as $\widetilde{\phi} = \overline{\rho\phi}/\bar{\rho}$. $+$ and $*$ indicate normalization by wall units and semilocal wall units, respectively. Fluctuations from the Reynolds- and Favre-averaged quantities are defined as ϕ' and ϕ'', respectively. According to our results, the compressibility factor in our cases significantly departs from 1, suggesting that strong

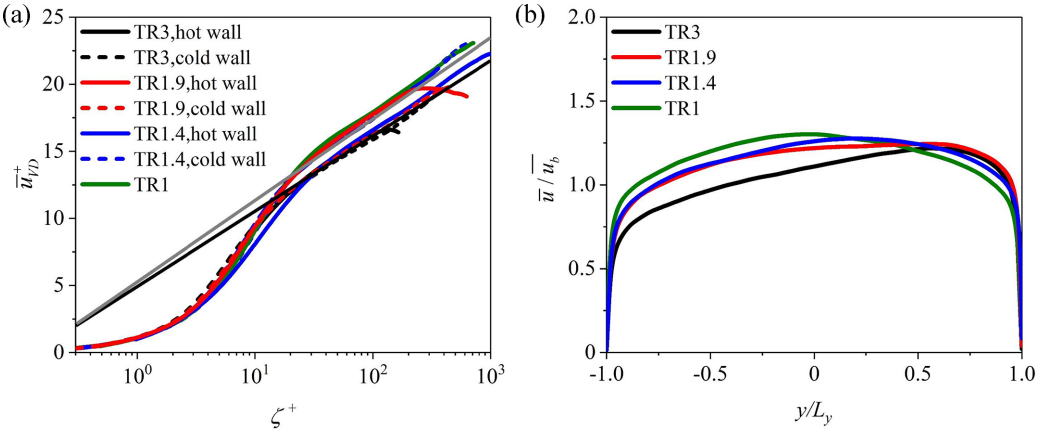

FIG. 1. (a) The van Driest transformed mean velocity profiles of all cases and the law of the wall, with the log law $\overline{u^+_{\mathrm{VD}}} = \log(\zeta^+)/\kappa + B$. $\kappa = 0.41$ and $B = 5$ for the black straight line and $\kappa = 0.38$, $B = 5.2$ for the gray straight line; (b) mean velocity $\bar{u}/\overline{u_b}$ as a function of y/L_y.

real-fluid effects exist in our simulation cases. We note that for all cases, the Mach number is less than 0.16, indicating that the configurations in all cases correspond to the low-speed flow regime. Moreover, the pressure change in the channels is very small (the instantaneous p/p_c changes by less than 0.5% within the whole channel). Hence the dominant effects are the variable properties present at low Mach numbers. Due to the more drastic density changes in the gaslike fluid, the density fluctuation and real-fluid effects near the hot wall are more pronounced than those near the cold wall.

In Fig. 1, we show the van Driest transformed and untransformed mean velocity profiles for all cases along with the law of the wall, which corresponds to the established logarithmic scaling. The comparison with the law of the wall suggests that the log law works reasonably well. According to Guo *et al.* [22], the lower and upper bounds of the log layer in transcritical flows are $\zeta^* > 30$ and $\zeta/L_{y,\max(\bar{u})} = 0.3$, respectively, with $L_{y,\max(\bar{u})}$ being the distance from the wall to the location of maximum $\bar{u}$. We give the upper bounds of the log layer (i.e., $\zeta^+_{\max}$ and $\zeta^*_{\max}$) for all cases in Table III in Appendix C. Hereafter, the range of ζ^* is $\zeta^* \in (30, \zeta^*_{\max})$ when we mention "the log layer."

A. Turbulent dissipation rate

This section focuses on investigating the real-fluid effects on turbulent dissipation in transcritical flows. The dissipation rate is defined as [26]

$$\varepsilon = \overline{\tau'_{ij}\frac{\partial u'_i}{\partial x_j}} \quad \text{with} \quad \tau_{ij} = \mu\left(\frac{\partial u_i}{\partial x_j} + \frac{\partial u_j}{\partial x_i}\right) - \frac{2}{3}\mu\frac{\partial u_k}{\partial x_k}\delta_{ij}. \tag{5}$$

To investigate the dominant factor of the dissipation rate, we decompose the dissipation rate (see Appendix A for the derivation) as

$$\varepsilon = \varepsilon_{\mathrm{I}} + \varepsilon_{\mathrm{II}} + \varepsilon_{\mathrm{III}} + \varepsilon_{\mathrm{IV}} + \varepsilon_{\mathrm{V}}, \tag{6}$$

where

$$\varepsilon_{\mathrm{I}} = \frac{1}{2}\overline{\mu}\overline{\omega'_{ij}\omega'_{ij}},$$

$$\varepsilon_{\mathrm{II}} = -\frac{2}{3}\overline{\mu}\overline{d'^2},$$

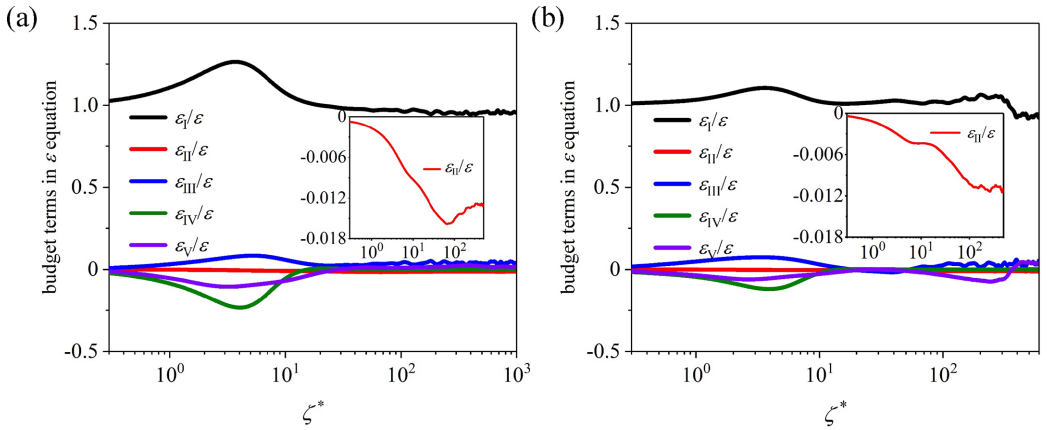

FIG. 2. Decomposition of dissipation rate of turbulent kinetic energy for case TR3. (a) Budget terms near the cold wall; (b) budget terms near the hot wall.

$$\varepsilon_{\mathrm{III}} = 2\overline{\mu}\,\overline{\frac{\partial u_i'}{\partial x_j}\frac{\partial u_j'}{\partial x_i}},$$

$$\varepsilon_{\mathrm{IV}} = \overline{\mu'\frac{\partial u_i'}{\partial x_j}\left(\frac{\partial \overline{u}_i}{\partial x_j} + \frac{\partial \overline{u}_j}{\partial x_i} - \frac{2}{3}\frac{\partial \overline{u_k}}{\partial x_k}\delta_{ij}\right)},$$

$$\varepsilon_{\mathrm{V}} = \overline{\mu'\frac{\partial u_i'}{\partial x_j}\left[\left(\frac{\partial u_i'}{\partial x_j} + \frac{\partial u_j'}{\partial x_i} - \frac{2}{3}\frac{\partial u_k'}{\partial x_k}\delta_{ij}\right)\right]},$$

and

$$\omega_{ij}' = \frac{\partial u_i'}{\partial x_j} - \frac{\partial u_j'}{\partial x_i}, \quad d' = \frac{\partial u_k'}{\partial x_k}, \tag{7}$$

where ε_{I} is the solenoidal term composed of the mean viscosity and the enstrophy, $\varepsilon_{\mathrm{II}}$ is the dilatational term related to the velocity divergence, $\varepsilon_{\mathrm{III}}$ captures the interactions between the mean viscosity and the derivative of velocity fluctuations, $\varepsilon_{\mathrm{IV}}$ and ε_{V} are terms related to the fluctuations in viscosity, and ω_{ij} is the vorticity. Fig. 2 presents the budget terms of Eq. (6). These results show that the dissipation rate is dominated by the solenoidal term ε_{I} in the log layer, which means that the dissipation is mostly generated by vortex stretching while the dilatational effect ($\varepsilon_{\mathrm{II}}$) is negligible. As reported by Huang *et al.* [26], the dilatational term is quite small in high-Mach-number compressible wall-bounded flow, and we thus conclude that the behavior of the dissipation at transcritical conditions is similar to that of compressible, high-speed wall-bounded flows at subcritical pressures. Interestingly, we find that the temperature-dependent variation in viscosity plays an important role on the dissipation in the viscous sublayer and the buffer layer. The mean viscosity tends to intensify the turbulent dissipation while the fluctuating viscosity attenuates the dissipation. A maximum magnitude of $\varepsilon_{\mathrm{IV}}$ and ε_{V} is observed at $\zeta^* \approx 5$.

1. Effect of variable density (dilatation)

We first examine the mean dilatation as well as its fluctuation [defined in Eq. (8)] in Fig. 3. In the log layer, the results in Fig. 3 show that the dilatation is negligible. As a result of this, $\varepsilon_{\mathrm{II}}$ is negligibly small in the log layer (see Fig. 2). In the near-wall layers, $\varepsilon_{\mathrm{II}}$ is far weaker than ε_{I}, as shown in Fig. 2. This indicates that dilatation is negligible compared with vorticity. Thus, although dilatation is more pronounced in the near wall layers, $\varepsilon_{\mathrm{II}}/\varepsilon$ is still negligible ($|\varepsilon_{\mathrm{II}}/\varepsilon| < 1.5\%$, as

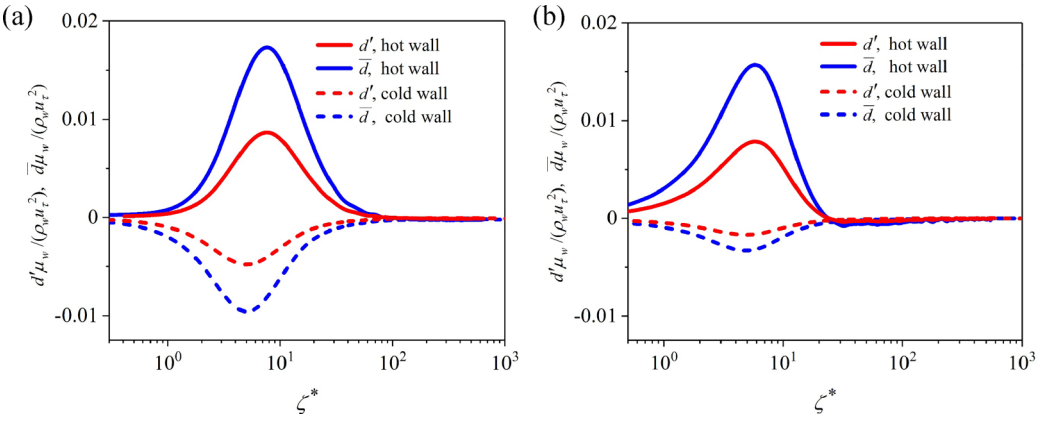

FIG. 3. Plots of mean dilatation $\bar{d}$ and root-mean-square values (rms) of fluctuating dilatation d'_{rms} in (a) TR3, (b) TR1.9.

shown in the inset graph in Fig. 2). The dilatation near the hot wall is larger in magnitude than that near the cold wall, implying more significant variable-density effects as fluctuating density increases,

$$\bar{d} = \frac{\partial \overline{u_i}}{\partial x_i}, \quad d' = \frac{\partial u_i'}{\partial x_i}. \tag{8}$$

2. *Effect of variable viscosity*

We proceed to examine the effects of the viscosity fluctuations on the dissipation rate in the near-wall layer. Fig. 4 shows the instantaneous structures of fluctuating vorticity and viscosity at $\zeta^* = 5$ (the wall-normal position where ε_{IV} and ε_{V} reach their peak values) and at $\zeta^* = 50$ (in the log layer with negligible ε_{IV} and ε_{V}) near the cold wall. It can be seen that the low-vorticity streaks correlate well with the streaks of high viscosity fluctuation, as shown by the red boxes inset in Figs. 4(a) and 4(c). In contrast, this behavior is not observed at $\zeta^* = 50$ [see Figs. 4(b) and 4(d)]. Since the dissipation rate is mainly generated by the vorticity, the strong correlation between the low-vorticity streaks and high-viscosity-fluctuation streaks implies that μ' attenuates ε. These structural observations are consistent with the above conclusions reached in the analysis of Eq. (6).

We will now examine the mechanism of the interactions between μ' and ε by analyzing the modulations on the transcritical turbulent structures via ε_{IV} and ε_{V}. Intensified unsteadiness of near-wall streaks along with stronger streamwise vortical structures were observed when the turbulent structures tilt with respect to the streamwise direction [27,28]. Thus, the influences of viscosity variations on vorticity and dissipation rate can be interpreted by the streamwise vortical structures. The orientation of the vortical structures is characterized by the real eigenvector of the fluctuating velocity gradient tensor [29]. Following the procedures given by Patel *et al.* [29], we investigate the inclination and tilting angles of the vortical structures. In Fig. 5, we show the PDFs of projection angle of vortical structures for case TR3, including the inclination angle with respect to the x-y plane [Fig. 5(a)] and the tilting angle with respect to the x-z plane [Fig. 5(b)]. It can be seen that the turbulent structures at $\zeta^* = 5$ have much lower PDFs of inclination angle higher than 10°. This means that turbulent structures at $\zeta^* = 5$ are characterized by a lower inclination angle compared to $\zeta^* = 10$ and 50. Similarly, for the tilting angle shown in Fig. 5(b), we find that when $\theta_{xz} < -10^\circ$ and $\theta_{xz} > 15^\circ$, the vortical structures at $\zeta^* = 5$ have lower PDFs of tilting angle, suggesting that the tilting of the vortical structures is reduced. According to Johansson *et al.* [27], the tilting of turbulent structures is induced by the near-wall cycles of streamwise vortices accompanied by strong near-wall turbulent shear. This is evidenced by the plots of fluctuating streamwise vorticity for

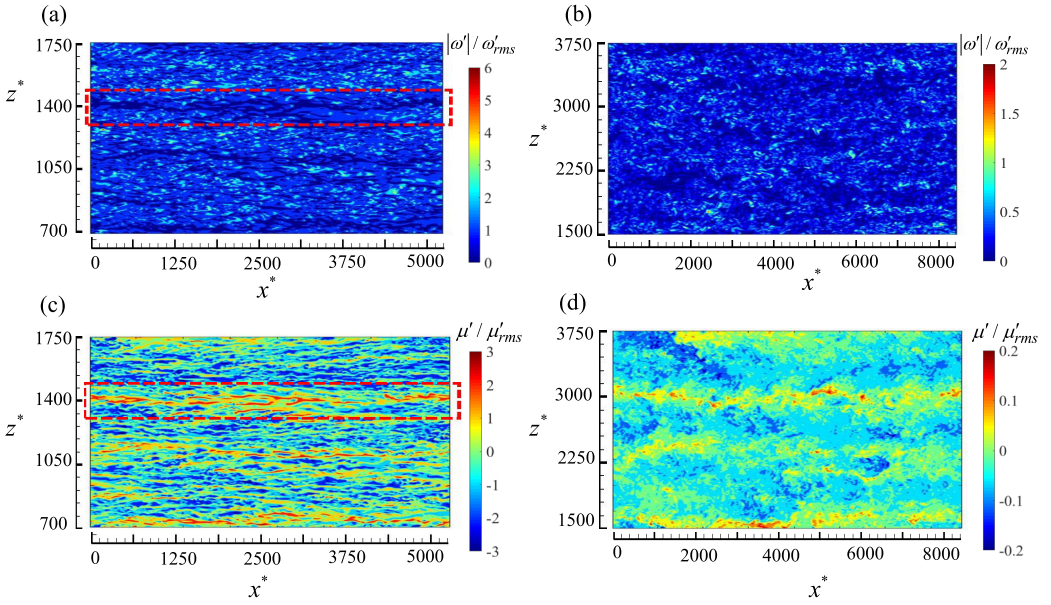

FIG. 4. Instantaneous contours of fluctuating vorticity and viscosity near the cold wall in TR3. The left panel and the right panel show the contours at $\zeta^* = 5$ and $\zeta^* = 50$, respectively. The red boxes indicate the low-vorticity streaks and the corresponding fluctuating viscosity streaks. The contours show the entire x-z extent of the computational domain.

different cases shown in Fig. 5(c); a local minimum of the streamwise vorticity can be observed at about $\zeta^* = 4$. Our investigation clarifies the mechanism of the influences of fluctuating viscosity on the generation of streamwise vorticity and dissipation rate, thus providing support for the real-fluid thermodynamic effects on dissipation rate in the near-wall layer.

According to our above analysis, the dissipation rate is dominated by the solenoidal term ε_{I}. Thus we extend our analysis by examining the enstrophy generation. For this, we decompose the production term of enstrophy, i.e., $\omega'_i\omega'_j s'_{ij}$, into six terms,

$$G = \omega'_i\omega'_j s'_{ij} = \underbrace{\omega'_x\omega'_x s'_{xx}}_{\mathrm{I}} + \underbrace{\omega'_y\omega'_y s'_{yy}}_{\mathrm{II}} + \underbrace{\omega'_z\omega'_z s'_{zz}}_{\mathrm{III}} + 2\underbrace{\omega'_x\omega'_y s'_{xy}}_{\mathrm{IV}} + 2\underbrace{\omega'_x\omega'_z s'_{xz}}_{\mathrm{V}} + 2\underbrace{\omega'_y\omega'_z s'_{yz}}_{\mathrm{VI}}, \tag{9}$$

where $s'_{ij} = (\partial u'_i/\partial x_j + \partial u'_j/\partial x_i)/2$ is the strain rate tensor. In Eq. (9), the terms I–III expressed by the interactions between the vorticity and the strain rates s_{xx}, s_{yy}, and s_{zz} represent the enstrophy produced by the linear strain, while the terms IV–VI related to s_{xy}, s_{yz}, and s_{xz} indicate the enstrophy generated by the shear strain.

Figure 6 displays the budget terms of the production of enstrophy in TR3 as a function of ζ^*. Since the budget term related to the enstrophy in the dissipation budget equation incorporates the local viscosity, we present the results of the enstrophy production weighted by local viscosity herein. The total production, $\overline{\bar{\mu}\omega'_i\omega'_j s'_{ij}}$, has a minimum value at $\zeta^* \approx 5$, at the edge of the viscous sublayer. We find that $\overline{\bar{\mu}\omega'_i\omega'_j s'_{ij}}$ abruptly decreases at the wall-normal position where $\varepsilon_{\mathrm{IV}}$ and ε_{V} reach their peak values, implying that the fluctuating viscosity attenuates the enstrophy production as well as the turbulent dissipation [see Fig. 6(a)]. Moreover, it can be seen in Fig. 6(b) that the budget terms related to the shear strain (i.e., terms IV–VI) also decrease at $\zeta^* \approx 4$. Unlike the behaviors

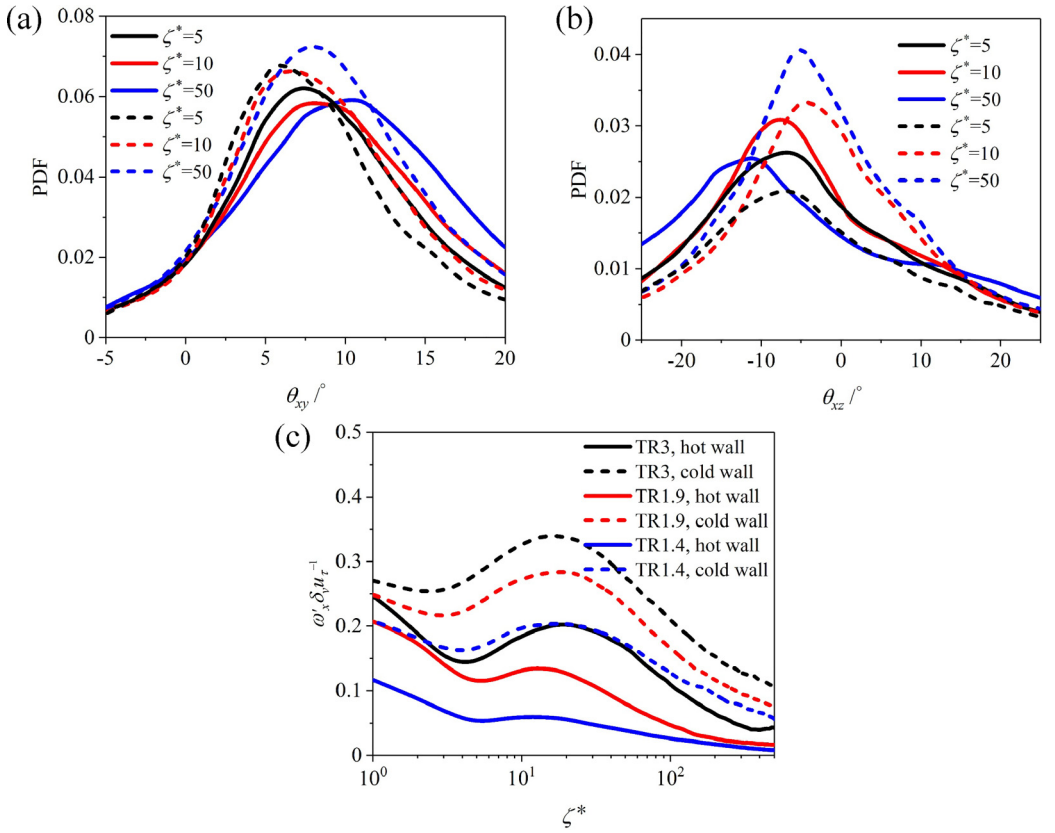

FIG. 5. (a) PDFs of inclination angle of vortical structures near both walls for case TR3, with solid lines and dashed lines indicating the profiles near the hot wall and the cold wall, respectively; (b) PDFs of tilting angle of vortical structures near both walls for case TR3; (c) rms of wall-scaled fluctuating streamwise vorticity for different cases.

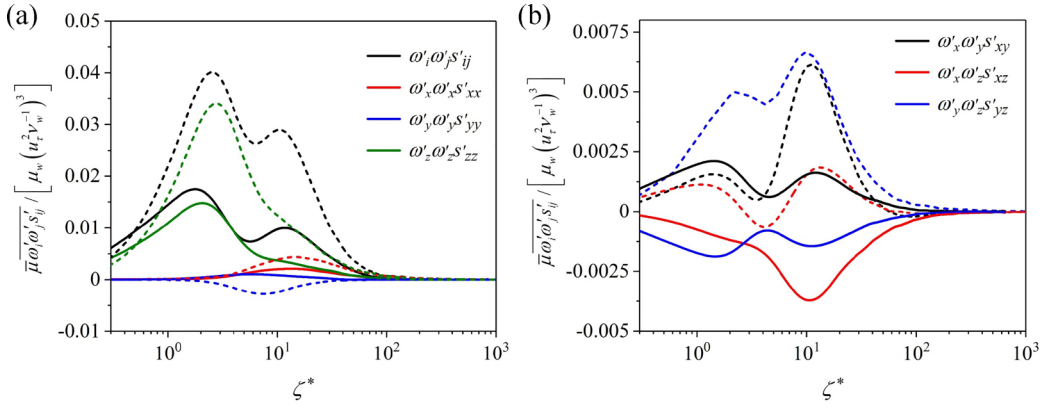

FIG. 6. Budget terms of viscosity weighted enstrophy production in TR3 as a function of ζ^*. (a) Production terms $\bar{\mu}\overline{\omega'_x \omega'_x s'_{xx}}$, $\bar{\mu}\overline{\omega'_y \omega'_y s'_{yy}}$, $\bar{\mu}\overline{\omega'_z \omega'_z s'_{zz}}$; (b) production terms $\bar{\mu}\overline{\omega'_x \omega'_y s'_{xy}}$, $\bar{\mu}\overline{\omega'_x \omega'_z s'_{xz}}$, $\bar{\mu}\overline{\omega'_y \omega'_z s'_{yz}}$. Solid lines indicate the hot wall profiles and dashed lines indicate the cold wall profiles.

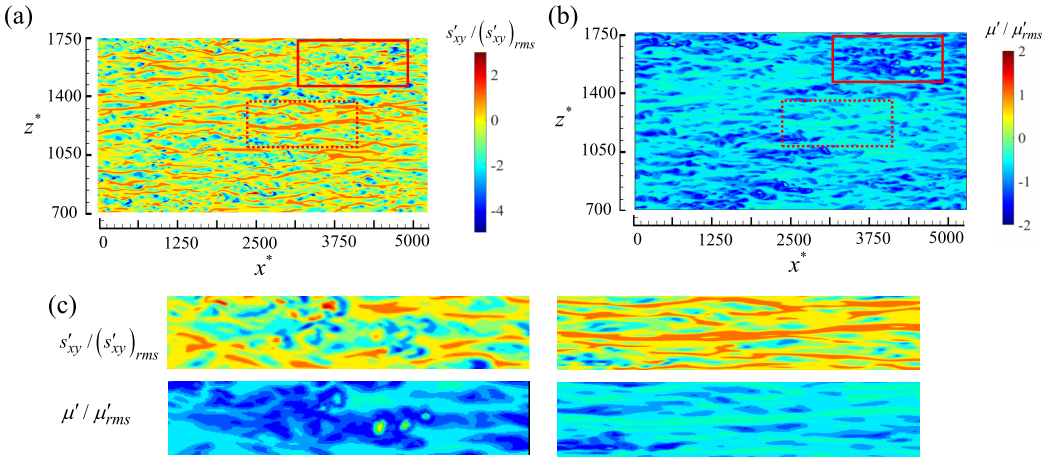

FIG. 7. Instantaneous wall-parallel snapshots of fluctuating shear strain and viscosity at $\zeta^* = 5$ near the hot wall in TR3. (a) Rescaled strain rate s'_{xy}; (b) rescaled fluctuating viscosity; (c) zoomed regions indicated by the superimposed red solid lines [left panel in (c)] and dashed lines [right panel in (c)].

of terms IV–VI, terms I–III are not affected by the increasing $\varepsilon_{\mathrm{IV}}$ and ε_{V} in the viscous sublayer [see Fig. 6(a)]. These observations suggest that in the viscous sublayer, the viscosity fluctuation reduces the enstrophy production by means of reducing the shear strain. As a result, the vorticity is weakened, which leads to the attenuated dissipation rate. Such a conclusion is further confirmed by the instantaneous contours of fluctuating viscosity and shear strain presented in Fig. 7. High $|\mu'|$ (or low $|\mu'|$) streaks correlate well with low $|s'_{xy}|$ (or high $|s'_{xy}|$) streaks, indicating the role of fluctuating viscosity on modulating the shear strain and the enstrophy production. According to the studies on the compressible or the variable-density mixing layer [30,31], the viscosity variation as well as its fluctuations are also negatively correlated with the enstrophy and dissipation rate. For the turbulent boundary layers with temperature-dependent viscosity, Lee *et al.* [32] and Zonta *et al.* [33] found that near the hot wall, the dissipation rate is increased as the decreasing viscosity or negative viscosity fluctuations. This is consistent with the present observations, i.e., the fluctuating viscosity tends to attenuate the dissipation rate in the viscous sublayer near the hot wall. Notably, we also find that fluctuating viscosity plays the same role near the cold wall.

B. Turbulent kinetic energy

Next, we examine the transport of TKE and the mixing length. The budget equation for TKE in compressible flow is given as [13]

$$\frac{\partial(\overline{\rho}\tilde{k})}{\partial t} + C = P + T_d + T_p + D_v - \varepsilon + M + \mathbf{\Pi}_d, \tag{10}$$

where C, P, T_d, T_p, D_v, ε, M, and $\mathbf{\Pi}_d$ are the contributions from convection, production, turbulent diffusion, velocity-pressure interaction, viscous diffusion, energy dissipation, mass flux contribution associated with density fluctuations, and pressure dilatation, with the following mathematical expressions:

$$C = \frac{\partial}{\partial x_j}(\bar{\rho}\tilde{u}_j\tilde{k}), \quad P = -\overline{\rho u_i'' u_j''}\frac{\partial \tilde{u}_i}{\partial x_j},$$

$$T_d = -\frac{\partial}{\partial x_j}\left(\frac{1}{2}\overline{\rho u_i'' u_i'' u_j''}\right), \quad T_p = -\frac{\partial}{\partial x_j}(\overline{p' u_j'}),$$

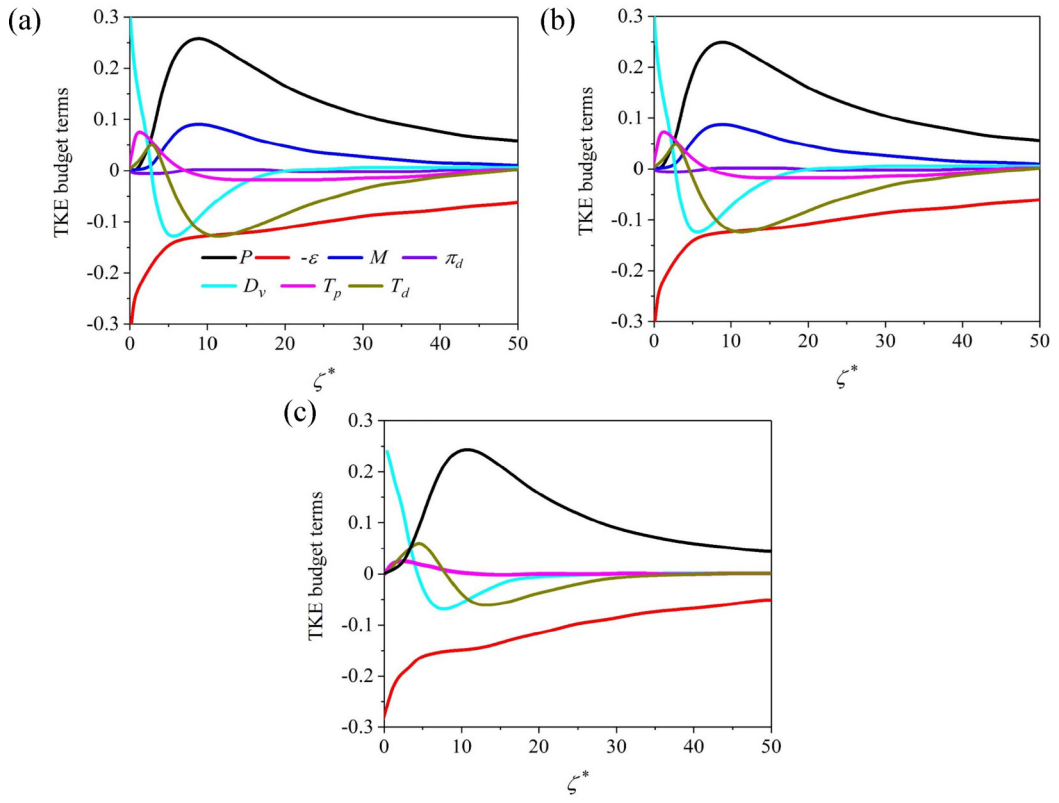

FIG. 8. Budget terms of the equation of turbulent kinetic energy normalized by τ_w^2/μ_w (wall scaling). (a) TR3 hot wall; (b) TR3 cold wall; (c) TR1.

$$D_v = \frac{\partial}{\partial x_j}(\overline{\tau'_{ij}u'_i}), \quad \varepsilon = \overline{\tau'_{ij}\frac{\partial u'_i}{\partial x_j}},$$
$$M = \overline{u''_i}\left(\frac{\partial \overline{\tau_{ij}}}{\partial x_j} - \frac{\partial \overline{p}}{\partial x_i}\right), \quad \mathbf{\Pi}_d = \overline{p'\frac{\partial u'_i}{\partial x_i}}.$$

Figure 8 shows the budget terms of TKE normalized by τ_w^2/μ_w (wall units) for different cases. In the log layer, the wall-scaled P^+ and ε^+ are approximately equal in magnitude, indicating the existence of a local equilibrium of TKE. We thus have

$$P = -\overline{\rho u''_i u''_j}\frac{\partial \tilde{u}_i}{\partial x_j} = \varepsilon. \tag{11}$$

In Sec. III E, we will use the local equilibrium property to establish the scaling law of the mixing length and the production term of TKE.

C. Turbulent heat fluxes

To gain further insight into the physical underpinning of heat transport, we calculate turbulent heat fluxes in transcritical flows using quadrant analysis. The four quadrants $Q1$, $Q2$, $Q3$, and $Q4$ are referred to as outward, ejection, inward, and sweep events, respectively [13]. Fig. 9 displays results from this quadrant analysis for wall-normal turbulent heat flux. As shown in Fig. 9(a), the turbulent wall-normal heat fluxes for the ejection events ($|\overline{\rho v'' H''_{\mathrm{Q1}}} + \overline{\rho v'' H''_{\mathrm{Q2}}}|_{\mathrm{TR3}}$) are noticeably lower than

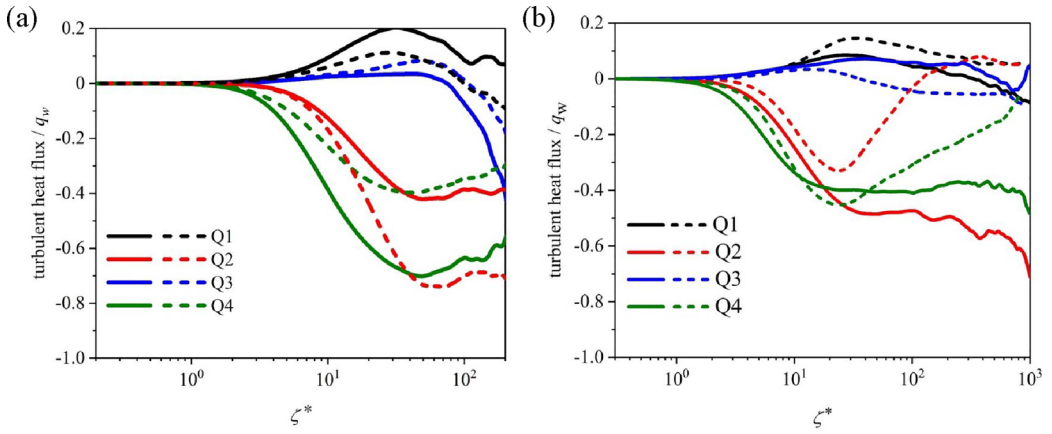

FIG. 9. Quadrant analysis on wall-normal Reynolds heat flux. (a) Hot wall profiles; the solid lines and dashed lines indicate $\overline{\rho v'' H''}$ and $\bar{\rho}\overline{v'' H''}$ for TR3, respectively; (b) cold wall profiles; solid lines, $\overline{\rho v'' H''}$ for TR3; dashed lines, $\overline{\rho v'' H''}$ for TR1.

those for the sweep events ($|\overline{\rho v'' H''_{Q3}} + \overline{\rho v'' H''_{Q4}}|_{TR3}$). Since the ejection events transfer near-wall gaslike hot fluids while the sweep events transfer liquidlike cold fluids to $\zeta^* = 50$, the thermal energy transported to $\zeta^* = 50$ by ejected gaslike fluids cannot completely compensate the thermal energy loss caused by the swept liquidlike fluids. This explains the formation of the highly skewed density probability density functions near the hot wall observed by Ma *et al.* [12]. In contrast, from Fig. 9(b) it can be seen that at $\zeta^* = 50$ near the cold wall in TR3, the turbulent wall-normal heat flux correlated with the ejection ($|\overline{\rho v'' H''_{Q1}} + \overline{\rho v'' H''_{Q2}}|_{TR3}$) is merely slightly higher than that related to sweep ($|\overline{\rho v'' H''_{Q3}} + \overline{\rho v'' H''_{Q4}}|_{TR3}$). Additionally, from Fig. 9(a) we also find that compared to the mean-density-related heat flux, the total heat flux $\overline{\rho v'' H''}$ increases for $Q1$ and $Q4$ events while it decreases for $Q2$ and $Q3$ events, implying that density fluctuations are enhancing the turbulent heat flux contributed from the high-speed streaks, while reducing the turbulent heat flux from the low-speed streaks.

D. Momentum fluctuation statistics

In this section we proceed to discuss the behaviors of momentum-fluctuation-related statistics under transcritical conditions, which is helpful for the development of the closure modeling of Favre equations. Following Patel *et al.* [18], the semilocally scaled second, third, and fourth order moments of momentum fluctuations are expressed as $\overline{\rho u''_\alpha u''_\alpha}/\tau_w$, $\overline{\rho^{1.5} u''_\alpha u''_\alpha u''_\alpha}/\tau_w^{1.5}$ and $\overline{\rho^2 u''_\alpha u''_\alpha u''_\alpha u''_\alpha}/\tau_w^2$ (where the subscript $\alpha = 1, 2, 3$ indicates the velocity component, Greek subscripts indicate any of the components without summation). These statistics can be decomposed into mean-density-related terms and density-fluctuation-related terms [18],

$$\overline{\rho u''_\alpha u''_\alpha} = \bar{\rho}\overline{u''_\alpha u''_\alpha} + \overline{\rho' u''_\alpha u''_\alpha}, \tag{12}$$

$$\overline{\rho^{1.5} u''_\alpha u''_\alpha u''_\alpha} \approx \bar{\rho}^{1.5}\overline{u''_\alpha u''_\alpha u''_\alpha} + 1.5\overline{\rho' u''_\alpha u''_\alpha u''_\alpha}, \tag{13}$$

$$\overline{\rho^2 u''_\alpha u''_\alpha u''_\alpha u''_\alpha} = \bar{\rho}^2\overline{u''_\alpha u''_\alpha u''_\alpha u''_\alpha} + 2\bar{\rho}\overline{\rho' u''_\alpha u''_\alpha u''_\alpha u''_\alpha} + \overline{\rho'^2 u''_\alpha u''_\alpha u''_\alpha u''_\alpha}. \tag{14}$$

In Fig. 10, we plot these terms for case TR3. Near the cold wall, the profiles of $\overline{\rho u''_\alpha u''_\alpha}$, $\overline{\rho^{1.5} u''_\alpha u''_\alpha u''_\alpha}$, and $\overline{\rho^2 u''_\alpha u''_\alpha u''_\alpha u''_\alpha}$ deviate slightly from the profiles of $\bar{\rho}\overline{u''_\alpha u''_\alpha}$, $\bar{\rho}^{1.5}\overline{u''_\alpha u''_\alpha u''_\alpha}$, and

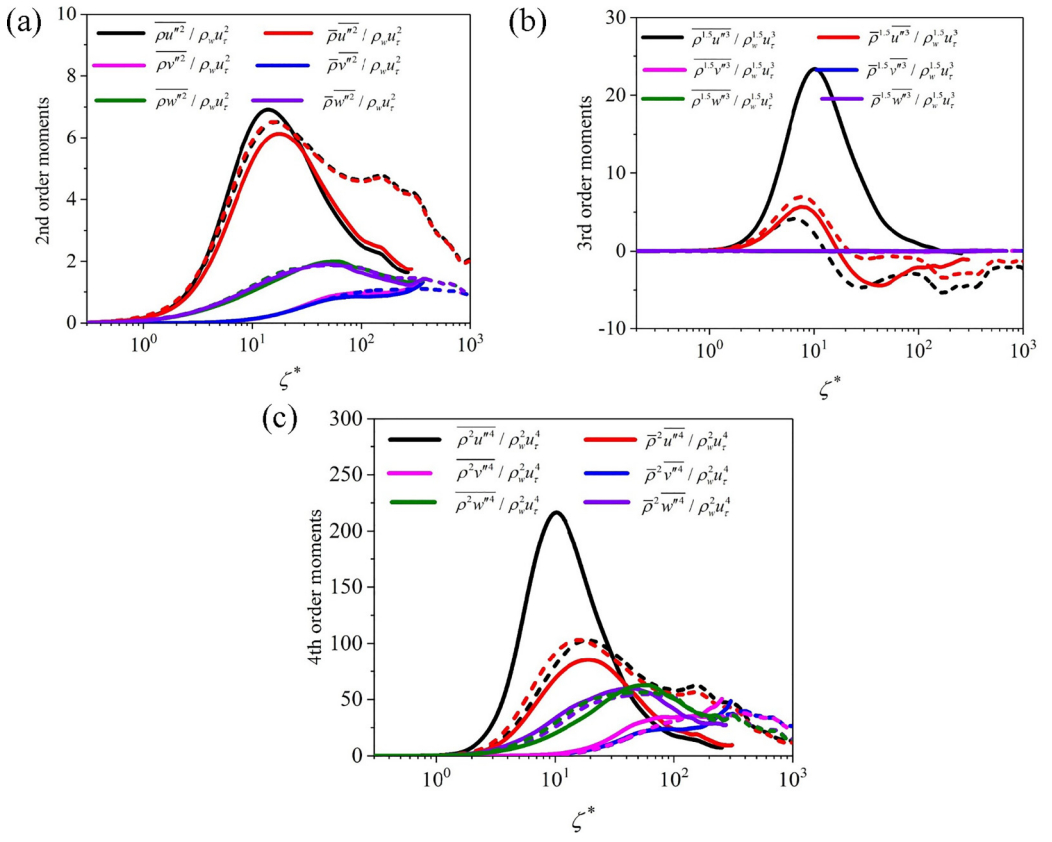

FIG. 10. Semilocally scaled (a) second-order statistics, (b) third-order statistics, and (c) fourth-order statistics of momentum-fluctuation as functions of ζ^* for case TR3. Solid lines: hot wall profiles; dashed lines: cold wall profiles. For clarity, the wall-normal and spanwise fourth order moments in (c) are multiplied by 10 and 5, respectively.

$\bar{\rho}^2\overline{u''_\alpha u''_\alpha u''_\alpha u''_\alpha}$, implying that the influence of the density fluctuations on momentum statistics is small. Interestingly, it can be seen that near the hot wall, the mean-density-related statistics deviate significantly from instantaneous-density-related statistics, implying the importance of density fluctuations on the balance of momentum-fluctuation statistics. This is distinctly different from the observations by Patel *et al.* [18].

E. Scaling laws based on the turbulent energy transport

1. Kolmogorov length scale

In Sec. III A, we find that the fluctuating vorticity dominates the generation of dissipation rate. Based on this physical underpinning of the dissipation rate at transcritical conditions, the expression for ε reduces to

$$\varepsilon \approx \tfrac{1}{2}\overline{\mu}\overline{\omega'_{ij}\omega'_{ij}}. \tag{15}$$

Hence, real-fluid effects owing to dilatation and fluctuation of thermodynamic quantities on turbulent dissipation are small, suggesting that Morkovin's hypothesis, which indicates that any difference between compressible turbulent boundary layer and incompressible turbulent boundary layer can be removed by incorporating the wall-normal variations of $\bar{\rho}$ and $\bar{\mu}$, applies to small-scale

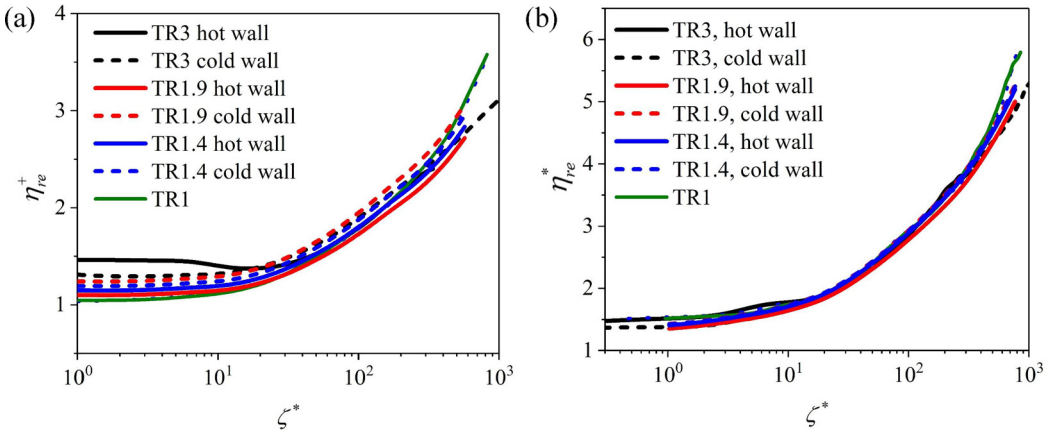

FIG. 11. Scaling laws of Kolmogorov length scale: (a) wall-scaled Kolmogorov length scale [Eq. (16a)] versus ζ^*; (b) semilocally scaled Kolmogorov length scale [Eq. (16b)] versus ζ^*.

structures in transcritical flows. This provides the possibility of extending the scaling laws of the Kolmogorov length scale from compressible high-Mach flows at subcritical pressures to transcritical flows. Assuming that Morkovin's hypothesis is valid on small scales, Zhang *et al.* [34] proposed the following scaling law for the rescaled Kolmogorov length scales in high-Mach flows at subcritical pressures,

$$\eta_{re}^{+} = \eta^{+}(\bar{\rho}^{+}/\bar{\mu}^{+})^{1/2} = (\varepsilon^{+}/\bar{\mu}^{+})^{-1/4}, \tag{16a}$$

$$\eta_{re}^{*} = \eta^{*}(\bar{\rho}^{+}/\bar{\mu}^{+})^{1/2} = (\varepsilon^{*}/\bar{\mu}^{+})^{-1/4}, \tag{16b}$$

where $\bar{\mu}^{+} = \bar{\mu}/\mu_w, \bar{\rho}^{+} = \bar{\rho}/\rho_w$. Note that $\varepsilon^{*} = \varepsilon u_\tau^{-2}(\bar{v}^2/u_\tau^{*2})\mu_w^{-1}$ denotes normalization using the semilocal viscous length scale δ_v^*. According to Zhang *et al.* [34], η_{re}^{+}, which is the transformation based on the wall scaling, is found to be effective in collapsing the profiles of the Kolmogorov length scale in high-Mach turbulence at subcritical pressures. Fig. 11 shows the normalized Kolmogorov length scale as a function of ζ^*. We observe that while η_{re}^{+} does not do well in collapsing the profiles, η_{re}^{*}, which is based on the semilocal transformation, performs better in collapsing the profiles in the log layer and the viscous sublayer.

2. Mixing length

Note that in turbulent boundary layers without curvature effects, the production of TKE mainly comes from the term $-\overline{\rho u'' v''}\frac{\partial \tilde{u}}{\partial \zeta}$. Thus Eq. (11) reduces to

$$-\overline{\rho u'' v''}\frac{\partial \tilde{u}}{\partial \zeta} = \overline{\rho} l_m^2 \left(\frac{\partial \tilde{u}}{\partial \zeta}\right)^3 = \varepsilon. \tag{17}$$

Solving Eq. (17) yields

$$l_m = \bar{\rho}\tilde{S}^{3/2}/\varepsilon. \tag{18}$$

with $S = -u'' v''$. This equation shows that a quantitative relation exists between mixing length and Kolmogorov length scale. According to Eq. (16b), $\varepsilon^{*} = \bar{\mu}^{+}(\eta_{re}^{*})^{-4}/\bar{\rho}^{+}$, the scaling law of the

normalized mixing length can then be written as

$$l_m^+ = (\tilde{S}^+)^2 \frac{\bar{\mu}^+}{\bar{\rho}^+} (\eta_{re}^*)^4, \tag{19}$$

where $l_m^+ = l_m \rho_w \tilde{S}^{1/2}/\mu_w$, $\tilde{S}^+ = \bar{\rho}\tilde{S}/\tau_w$ and τ_w is the wall shear stress. In the log layer, $\tilde{S}^+$ is derived from a stress balance analysis in the channel. Similar to the heat flux balance derivation in Guo *et al.* [22], by integrating the streamwise momentum equation in the wall-normal direction and averaging over time and homogeneous directions, we have (note that the present DNS shows a negligible contribution from $\bar{\rho}\tilde{u}\tilde{v}$ compared with other terms in the channel flows)

$$-\int_0^\zeta \overline{\frac{\partial p}{\partial x}} d\varphi + \int_0^\zeta \overline{\frac{\partial \tau_{1i}}{\partial x_i}} d\varphi - \overline{\rho u'' v''} = 0, \tag{20}$$

where $\tau_{1i} = \mu(\partial u/\partial x_i + \partial u_i/\partial x - 2\delta_{1i}\partial u_k/3\partial x_k)$ and φ is the wall-normal integral variable. With this, Eq. (20) can be rewritten as

$$-\int_0^\zeta \frac{\partial \bar{p}}{\partial x} d\varphi + \int_0^\zeta \frac{\partial}{\partial x_i}\overline{\left[\mu\left(\frac{\partial u}{\partial x_i} + \frac{\partial u_i}{\partial x}\right)\right]} d\varphi - \frac{2}{3}\int_0^\zeta \frac{\partial}{\partial x_i}\left(\overline{\mu \frac{\partial u_k}{\partial x_k}}\delta_{1i}\right) d\varphi - \overline{\rho u'' v''} = 0. \tag{21}$$

Note that in this equation, the turbulent shear stress $-\overline{\rho u'' v''}$, the pressure gradient term $-\int_0^\zeta \partial\bar{p}/\partial x d\varphi$, the viscous stress term $\int_0^\zeta \frac{\partial}{\partial x_i}\overline{[\mu(\frac{\partial u}{\partial x_i} + \frac{\partial u_i}{\partial x})]} d\varphi$, and the divergence term $-\frac{2}{3}\int_0^\zeta \frac{\partial}{\partial x_i}(\overline{\mu \frac{\partial u_k}{\partial x_k}}\delta_{1i}) d\varphi$ are present. In order to simply this equation, we calculate each budget term in Eq. (21), as shown in Fig. 12. Results from Fig. 12(a) show that the mean pressure remains nearly constant along the wall-normal directions. Thus the pressure gradient term can be written as

$$-\int_0^\zeta \overline{\frac{\partial p}{\partial x}} d\varphi = -\int_0^\zeta \frac{d\bar{p}}{dx} d\varphi. \tag{22}$$

In the streamwise direction, the wall shear stress balances the pressure gradient, yielding

$$\frac{\tau_{\mathrm{w,cold}} + \tau_{\mathrm{w,hot}}}{2L_y} = -\frac{d\bar{p}}{dx}. \tag{23}$$

Figures 12(b) and 12(c) show the viscous stress term and the divergence term, respectively. When assessing the absolute value of the magnitude across both cases, it can be seen that the divergence term is two orders of magnitude smaller than the viscous stress term in the log layer, and thus does not provide a significant contribution. With this simplification and neglecting the viscous stress term $\overline{\mu(\partial u/\partial y)}$ in the log layer, the streamwise momentum equation can be rewritten as

$$\frac{\tau_{\mathrm{w,hot}} + \tau_{\mathrm{w,cold}}}{2L_y}\zeta - \tau_w - \overline{\rho u'' v''} = 0. \tag{24}$$

Using the wall shear stress to rescale Eq. (24) and transforming it into a semilocally scaled form, we obtain the final expression for $\tilde{S}^+$:

$$\left(1 - \frac{\zeta}{2L_y}\right) - \frac{\tau_{w,\mathrm{hot}}}{\tau_{w,\mathrm{cold}}}\frac{\zeta}{2L_y} = \left(1 - \frac{\zeta^*}{2\mathrm{Re}_\tau^*}\right) - \frac{\tau_{w,\mathrm{hot}}}{\tau_{w,\mathrm{cold}}}\frac{\zeta^*}{2\mathrm{Re}_\tau^*} = \tilde{S}^+ \text{ (near the cold wall)}, \tag{25a}$$

$$\left(1 - \frac{\zeta}{2L_y}\right) - \frac{\tau_{w,\mathrm{cold}}}{\tau_{w,\mathrm{hot}}}\frac{\zeta}{2L_y} = \left(1 - \frac{\zeta^*}{2\mathrm{Re}_\tau^*}\right) - \frac{\tau_{w,\mathrm{cold}}}{\tau_{w,\mathrm{hot}}}\frac{\zeta^*}{2\mathrm{Re}_\tau^*} = \tilde{S}^+ \text{(near the hot wall)} \tag{25b}$$

with $\mathrm{Re}_\tau^* = \bar{\rho}u_\tau^* L_y/\bar{\mu}$ the semilocal friction Reynolds number.

Figure 13 shows the semilocal mixing lengths profiles, as well as the mixing lengths predicted by our Eq. (19). Compared to the semilocal scaling, which has difficulty in consistently characterizing the mixing length profiles in conditions with large density ratios [see Fig. 13(a)], our scaling law

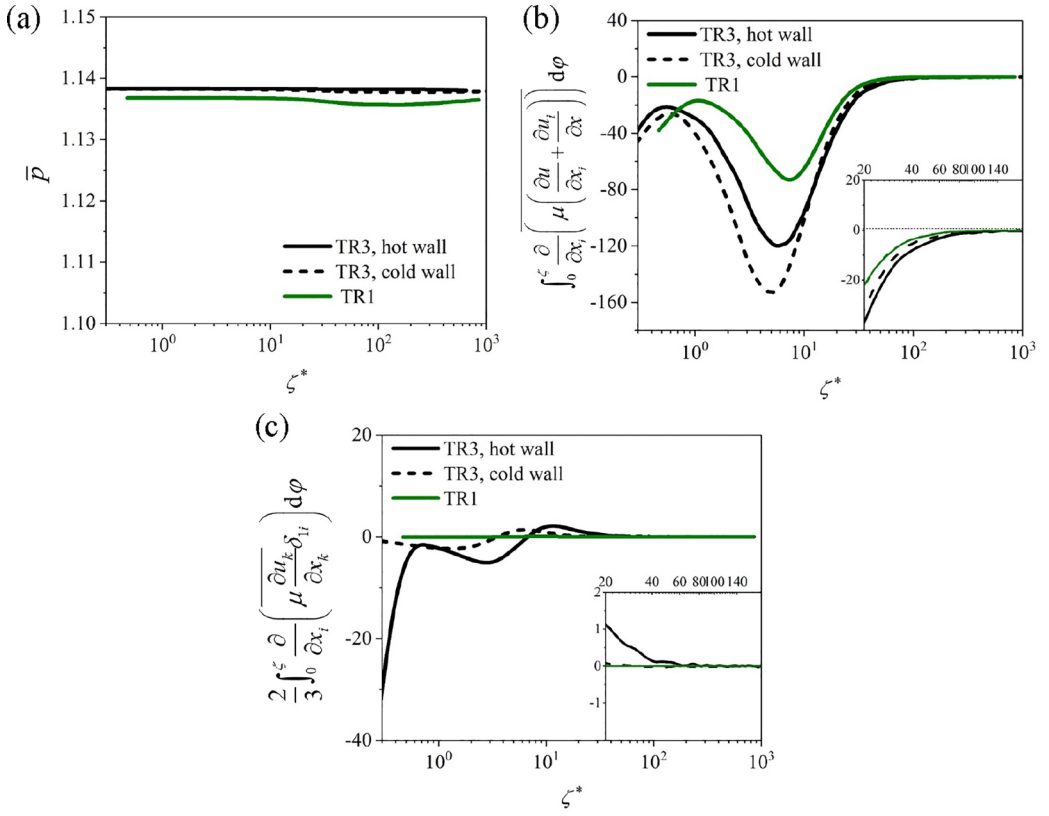

FIG. 12. Budget term analysis in Eq. (21). (a) Mean pressure $\bar{p}/p_c$; (b) viscous stress term; (c) divergence term.

collapses the data near the hot wall of TR3 into the single line in the log layer [see Fig. 13(b)]. We note that the discrepancy of the data for $\zeta^* < 20$ is related to the significant viscous dissipation in the near-wall layers.

3. TKE budget terms

We finally discuss the scaling laws of TKE budget terms. As in Eq. (16b), the scaling law of the dissipation rate is given by

$$(\varepsilon^*/\bar{\mu}^+)^{-1/4} = f(\zeta^*), \varepsilon^* = \bar{\mu}^+(\eta_{re}^*)^{-4} = \bar{\mu}^+[f(\zeta^*)]^{-4}, \tag{26}$$

with $f(\zeta^*)$ (i.e., the η_{re}^* with generalizability) a universal function of ζ^* plotted in Fig. 11(b). To examine other TKE budget terms related to the variations of the thermodynamic properties, we decompose them (including production term P, turbulent diffusion term T_d, viscous diffusion D_v, and mass flux contribution term M) into the mean thermodynamic-properties ($\bar{\rho}$ and $\bar{\mu}$) and fluctuating thermodynamic property (ρ' and μ') related terms, as shown in Eqs. (27)–(30):

$$P = -\overline{\rho u_i'' u_j''}\frac{\partial \tilde{u}_i}{\partial x_j} = \underbrace{\left(-\bar{\rho}\overline{u_i'' u_j''}\frac{\partial \tilde{u}_i}{\partial x_j}\right)}_{P_{k1}} + \underbrace{\left(-\overline{\rho' u_i'' u_j''}\frac{\partial \tilde{u}_i}{\partial x_j}\right)}_{P_{k2}}, \tag{27}$$

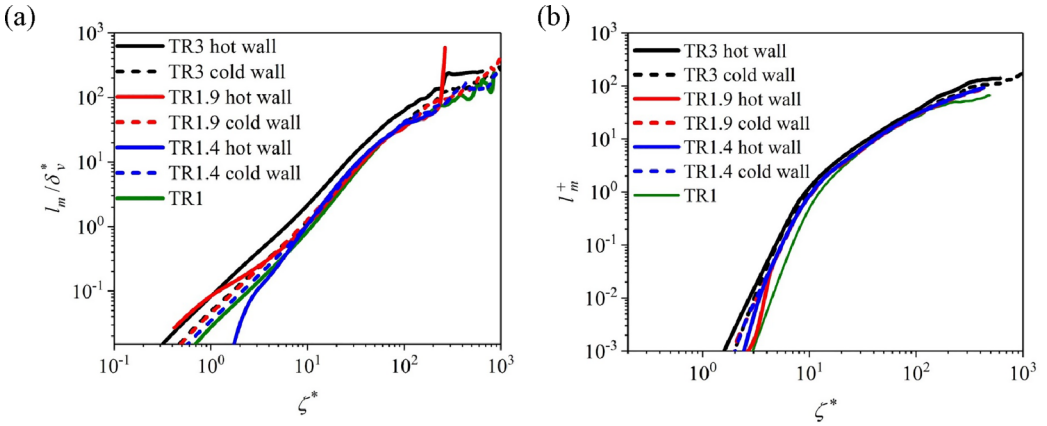

FIG. 13. (a) Semilocally scaled mixing lengths l_m/δ_v^* as a function of ζ^*; (b) normalized mixing length profiles predicted by our scaling law [Eq. (19)].

$$T_d = -\frac{\partial}{\partial x_j}\left(\frac{1}{2}\overline{\rho u_i'' u_i'' u_j''}\right) = \underbrace{\left[-\frac{\partial}{\partial x_j}\left(\frac{1}{2}\bar{\rho}\overline{u_i'' u_i'' u_j''}\right)\right]}_{T_{d1}} + \underbrace{\left[-\frac{\partial}{\partial x_j}\left(\frac{1}{2}\overline{\rho' u_i'' u_i'' u_j''}\right)\right]}_{T_{d2}}, \tag{28}$$

$$D_v = \frac{\partial}{\partial x_j}(\overline{\tau_{ij}' u_i'}) = \underbrace{\frac{\partial}{\partial x_j}\left[\overline{\mu} u_i'\left(\frac{\partial u_i'}{\partial x_j} + \frac{\partial u_j'}{\partial x_i} - \frac{2}{3}\frac{\partial u_k'}{\partial x_k}\delta_{ij}\right)\right]}_{D_{v1}} + \underbrace{\frac{\partial}{\partial x_j}\left[\mu' u_i'\left(\frac{\partial \overline{u}_i}{\partial x_j} + \frac{\partial \overline{u}_j}{\partial x_i} - \frac{2}{3}\frac{\partial \overline{u_k}}{\partial x_k}\delta_{ij}\right)\right]}_{D_{v2}}$$

$$+ \underbrace{\frac{\partial}{\partial x_j}\left[\mu' u_i'\left(\frac{\partial u_i'}{\partial x_j} + \frac{\partial u_j'}{\partial x_i} - \frac{2}{3}\frac{\partial u_k'}{\partial x_k}\delta_{ij}\right)\right]}_{D_{v3}}, \tag{29}$$

$$M = \overline{u_i''}\left(\frac{\partial \overline{\tau_{ij}}}{\partial x_j} - \frac{\partial \overline{p}}{\partial x_i}\right) = -\frac{\overline{\rho' u_i'}}{\bar{\rho}}\left(\frac{\partial \overline{\tau_{ij}}}{\partial x_j} - \frac{\partial \overline{p}}{\partial x_i}\right)$$

$$= \underbrace{-\frac{\overline{\rho' u_i'}}{\bar{\rho}}\frac{\partial}{\partial x_j}\left[\overline{\mu}\left(\frac{\partial \overline{u}_i}{\partial x_j} + \frac{\partial \overline{u}_j}{\partial x_i}\right)\right]}_{M_1} \underbrace{-\frac{\overline{\rho' u_i'}}{\bar{\rho}}\frac{\partial}{\partial x_j}\left[\overline{\mu'\left(\frac{\partial u_i'}{\partial x_j} + \frac{\partial u_j'}{\partial x_i}\right)}\right]}_{M_2}$$

$$+ \underbrace{\frac{\overline{\rho' u_i'}}{\bar{\rho}}\frac{\partial}{\partial x_j}\left[\frac{2}{3}\delta_{ij}\overline{\mu}\frac{\partial \overline{u}_k}{\partial x_k}\right]}_{M_3} + \underbrace{\frac{\overline{\rho' u_i'}}{\bar{\rho}}\frac{\partial}{\partial x_j}\left[\frac{2}{3}\delta_{ij}\overline{\mu' \frac{\partial u_k'}{\partial x_k}}\right]}_{M_4} + \cdots. \tag{30}$$

We note that P_{k2}, T_{d2}, and M_1–M_4 are associated with ρ', D_{v2} and D_{v3} are induced by μ', while other terms only depend on mean thermodynamic properties. Taking TR3 for instance, we show the decomposition terms of the TKE budgets in Fig. 14. Overall, the fluctuating thermodynamic property related term (P_{k2}) have an insignificant contribution (less than 10% across the majority of the channel) to the total production term P_k [see Fig. 14(a)]. This provides support that the scaling laws of P and ε can be established properly by solely accounting for the mean thermodynamic property changes, indicating that the Morkovin's hypothesis applies to the TKE production as well as its dissipation.

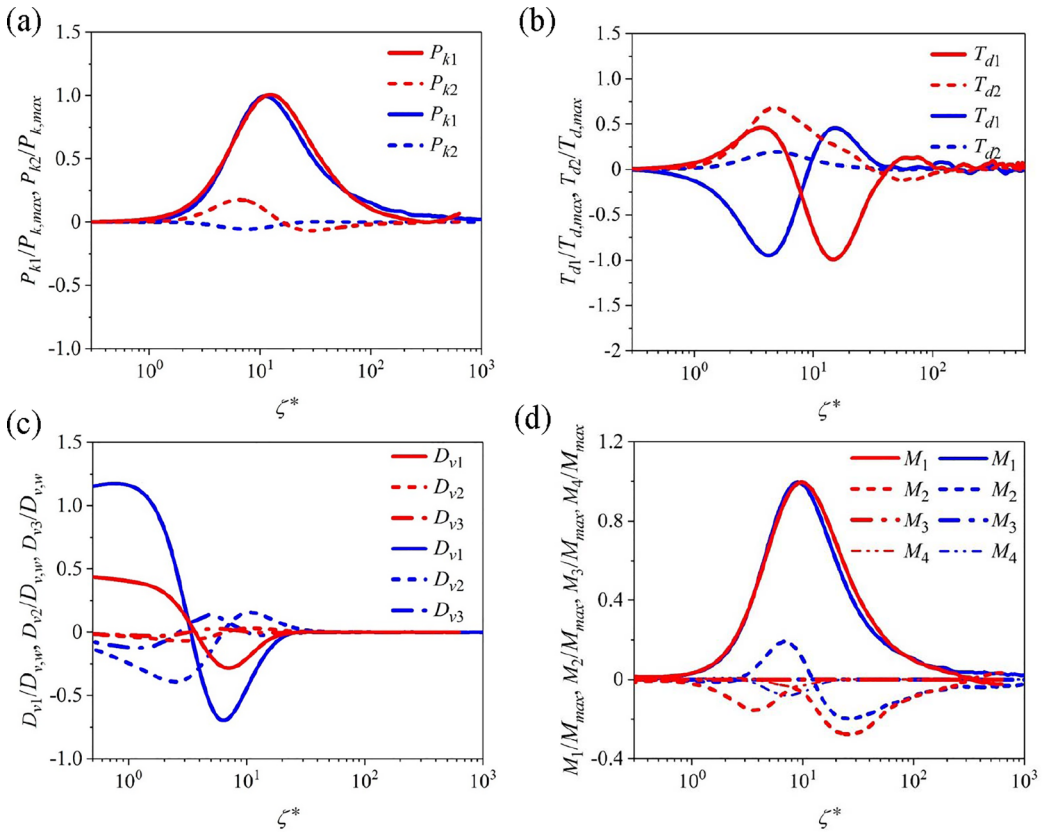

FIG. 14. Decomposition of the TKE budget terms in Eqs. (27)–(30) for TR3. (a) Production term P_k; (b) turbulent diffusion term T_d; (c) viscous diffusion D_v; (d) mass flux contribution term M. Red lines: near the hot wall; blue lines: near the cold wall. Results in (c) are rescaled by D_v at the wall, while results in (a), (b), and (d) are rescaled by the maximum of P_k, T_d, and M, respectively.

In the previous discussions, we justify that the dissipation rate induced by fluctuating thermodynamic properties is approximately zero in the log layer. As in Eq. (11), TKE production and dissipation are also in balance. The scaling law of TKE production in the log layer can be obtained based on the local equilibrium of P and ε:

$$P^* = (\bar{\rho}^+)^{1/2}(\eta^*_{re})^{-4} = (\bar{\rho}^+)^{1/2}[f(\zeta^*)]^{-4}, \tag{31}$$

where $P^* = P\rho_w^{-1}u_\tau^{-3}[\bar{\mu}/(\bar{\rho}u^*_\tau)]$. Equation (31) only contains the variations of mean thermodynamic properties, thus supporting that P_k is a solenoidal quantity. Differently, the fluctuating-thermodynamic-property related terms of T_d, D_v, and M are now noticeable as the main contribution terms [see Figs. 14(b)–14(d)]. This suggests that the scaling law, which ignores the fluctuating thermodynamic properties, is physically invalid when predicting these budget terms.

The results from this study show that thermodynamic fluctuations do not affect the TKE production and dissipation in the log layer. This in turn implies that real-fluid effects do not affect the local equilibrium of TKE which was originally shown for wall-bounded flows at subcritical pressures. However, real-fluid thermodynamic effects may result in the failure of some critical assumptions, such as the invariance of dissipation rate and Reynolds shear stress [22,35]. This indicates that real-fluid thermodynamic effects are dominant over the equilibrium assumption in the context of mean velocity transformations so that the former effects are first order. This provides insight to

explain the failure of mean velocity scaling at transcritical conditions [35], in which a transformation is developed that incorporates local equilibrium in the log layer.

IV. CONCLUSIONS

In this study, we analyze the turbulent energy transport and scaling laws for transcritical flows to shed light on developing effective turbulence models for transcritical flows in realistic engineering applications. To this end, direct numerical simulation data for transcritical channel flows with density ratio values of up to $O(20)$ are analyzed. Specifically, we examine the turbulent dissipation, turbulent kinetic energy budgets, turbulent heat flux, and momentum-fluctuation statistics.

The budget analysis shows that the dissipation rate of turbulent kinetic energy is dominated by the solenoidal term associated with enstrophy in the log layer, while the contributions from dilatation are insignificant. The variable viscosity plays an important role on the dissipation in the viscous sublayer; the mean viscosity tends to increase turbulent dissipation while the viscosity fluctuations weaken the dissipation. The viscosity fluctuations in the near-wall layer modulate the generation of streamwise vorticity by weakening the tilting of the turbulent structures. It is found that fluctuations in viscosity attenuate the dissipation rate by reducing the shear strain and the enstrophy production in the viscous sublayer. Although real-fluid effects have significant influence on the TKE budgets, local equilibrium of TKE transport in transcritical flows is verified in the log layer.

Near the hot wall, the wall-normal turbulent heat flux correlated with the sweep events that carries cold fluids is higher than that related to ejection events that entrains hot fluid, resulting in the highly skewed PDFs of temperature. The density-fluctuation-related terms momentum-fluctuation statistics are significant, implying the non-negligible role of density fluctuations on the balance of momentum-fluctuation statistics.

Considering that the dominant mechanism for dissipation rate in high-Mach turbulence and transcritical flows is similar in the log layer, we extend the scaling law of Kolmogorov length scale from high-Mach flows to transcritical flows. For the TKE budget terms, the scaling laws for P and ε are proposed based on their solenoidal behavior; the fluctuating-thermodynamic properties contribute noticeably to T_d, D_v, and M, revealing that the scaling law which merely considers variations of mean thermodynamic properties under the premise of Mokovin's hypothesis is invalid.

ACKNOWLEDGMENTS

This work was supported by the U.S. Department of Energy Office of Science with Award No. DE-SC0021129 and China's National Natural Science Foundation with Award No. 51888103.

APPENDIX A: DERIVATION OF THE DECOMPOSITION OF DISSIPATION RATE

Here we show the derivation of the decomposition of dissipation rate at transcritical conditions. From Eq. (5), the mean and fluctuating values of τ_{ij} are written as

$$\overline{\tau_{ij}} = \overline{\mu}\left(\frac{\partial \overline{u}_i}{\partial x_j} + \frac{\partial \overline{u}_j}{\partial x_i}\right) + \overline{\mu'\left(\frac{\partial u_i'}{\partial x_j} + \frac{\partial u_j'}{\partial x_i}\right)} - \frac{2}{3}\overline{\mu}\frac{\partial \overline{u}_k}{\partial x_k}\delta_{ij} - \frac{2}{3}\overline{\mu'\frac{\partial u_k'}{\partial x_k}}\delta_{ij}, \tag{A1}$$

$$\begin{aligned}\tau_{ij}' = {} & \overline{\mu}\left(\frac{\partial u_i'}{\partial x_j} + \frac{\partial u_j'}{\partial x_i} - \frac{2}{3}\frac{\partial u_k'}{\partial x_k}\delta_{ij}\right) + \mu'\left(\frac{\partial \overline{u}_i}{\partial x_j} + \frac{\partial \overline{u}_j}{\partial x_i} - \frac{2}{3}\frac{\partial \overline{u_k}}{\partial x_k}\delta_{ij}\right) \\ & + \left[\mu'\left(\frac{\partial u_i'}{\partial x_j} + \frac{\partial u_j'}{\partial x_i} - \frac{2}{3}\frac{\partial u_k'}{\partial x_k}\delta_{ij}\right)\right].\end{aligned} \tag{A2}$$

TABLE II. Grid resolutions in wall units at both walls and at the center of the channel, with $\eta_T = \eta_u/\sqrt{\mathrm{Pr}^*}$ the thermal Kolmogorov length scale, η_u the Kolmogorov length scale, and $\mathrm{Pr}^* = \overline{c_p}\bar{\mu}/\bar{\lambda}$ the local Prandtl number, with c_p the specific heat, μ the dynamic viscosity, and λ the thermal conductivity. The overbar indicates Reynolds average.

Cases		$(\Delta x)^+$	$(\Delta y)^+_{\mathrm{max}}$	$(\Delta y)^+_{\mathrm{min}}$	$(\Delta z)^+$	$(\Delta x/\eta_u)_{\mathrm{center}}$	$(\Delta y/\eta_u)_{\mathrm{center}}$	$(\Delta z/\eta_u)_{\mathrm{center}}$	$(\Delta x/\eta_T)_{\mathrm{center}}$	$(\Delta y/\eta_T)_{\mathrm{center}}$	$(\Delta z/\eta_T)_{\mathrm{center}}$
TR3	hot wall	4.89	4.64	0.2	3.26	3.8	3.3	2.5	8.9	8.2	5.9
	cold wall	7.09	6.73	0.29	4.73						
TR1.9	hot wall	10.21	9.68	0.42	6.81	2.7	2.6	1.8	5.0	4.5	3.3
	cold wall	7.32	6.95	0.30	4.88						
TR1.4	hot wall	22.90	21.72	0.94	15.26	2.5	2.5	1.7	3.7	3.8	2.5
	cold wall	8.01	7.60	0.33	5.34						
TR1		11.4	10.8	0.47	7.6	2.4	2.3	1.6	3.6	3.0	2.4

Therefore, the expression for dissipation rate can be written as

$$\varepsilon = \left(\overline{\mu}\overline{\frac{\partial u_i'}{\partial x_j}\frac{\partial u_i'}{\partial x_j}} + \overline{\mu}\overline{\frac{\partial u_i'}{\partial x_j}\frac{\partial u_j'}{\partial x_i}}\right) - \frac{2}{3}\overline{\mu}\overline{\frac{\partial u_i'}{\partial x_i}\frac{\partial u_k'}{\partial x_k}}$$
$$+ \overline{\mu'\frac{\partial u_i'}{\partial x_j}\left(\frac{\partial \overline{u}_i}{\partial x_j} + \frac{\partial \overline{u}_j}{\partial x_i} - \frac{2}{3}\frac{\partial \overline{u_k}}{\partial x_k}\delta_{ij}\right)} + \overline{\mu'\frac{\partial u_i'}{\partial x_j}\left(\frac{\partial u_i'}{\partial x_j} + \frac{\partial u_j'}{\partial x_i} - \frac{2}{3}\frac{\partial u_k'}{\partial x_k}\delta_{ij}\right)}. \tag{A3}$$

Using the modulus of the vorticity fluctuation

$$|\omega'| = \left[\overline{\left(\frac{\partial u'}{\partial y} - \frac{\partial v'}{\partial x}\right)^2} + \overline{\left(\frac{\partial u'}{\partial z} - \frac{\partial w'}{\partial x}\right)^2} + \overline{\left(\frac{\partial v'}{\partial z} - \frac{\partial w'}{\partial y}\right)^2}\right]^{1/2}$$

and the relation

$$\overline{\frac{\partial u_i'}{\partial x_j}\frac{\partial u_i'}{\partial x_j}} + \overline{\frac{\partial u_i'}{\partial x_j}\frac{\partial u_j'}{\partial x_i}} = |\omega'|^2 + 2\overline{\frac{\partial u_i'}{\partial x_j}\frac{\partial u_j'}{\partial x_i}},$$

we have

$$\varepsilon = \overline{\mu}|\omega'|^2 + 2\overline{\mu}\overline{\frac{\partial u_i'}{\partial x_j}\frac{\partial u_j'}{\partial x_i}} - \frac{2}{3}\overline{\mu}\overline{(\boldsymbol{\nabla}\cdot u')^2}$$
$$+ \overline{\mu'\frac{\partial u_i'}{\partial x_j}\left(\frac{\partial \overline{u}_i}{\partial x_j} + \frac{\partial \overline{u}_j}{\partial x_i} - \frac{2}{3}\frac{\partial \overline{u_k}}{\partial x_k}\delta_{ij}\right)} + \overline{\mu'\frac{\partial u_i'}{\partial x_j}\left(\frac{\partial u_i'}{\partial x_j} + \frac{\partial u_j'}{\partial x_i} - \frac{2}{3}\frac{\partial u_k'}{\partial x_k}\delta_{ij}\right)}, \tag{A4}$$

which is Eq. (6).

Based on the Helmholtz decomposition [36], Sarkar *et al.* [37] proposed a way to decompose ε into a solenoidal part ε_s and a dilatational part ε_d; the expressions of ε_s and ε_d in inhomogeneous flow are given as

$$\varepsilon_s = \tfrac{1}{2}\overline{\mu}\overline{\omega_{ij}'\omega_{ij}'}, \quad \varepsilon_c = -\tfrac{2}{3}\overline{\mu}\overline{d'^2}. \tag{A5}$$

A comparison with Eq. (6) shows that the solenoidal and dilatational budget terms in Eq. (6) are the same as those derived by the Helmholtz decomposition. To further confirm this, we can rearrange Eq. (6) using the Helmholtz decomposition. Since the solenoidal and the dilatational fluctuating velocities satisfy $\boldsymbol{\nabla}\cdot\mathbf{u}'_s = 0$ and $\boldsymbol{\nabla}\times\mathbf{u}'_c = 0$, we have

$$\varepsilon_{\mathrm{I}} = \frac{1}{2}\bar{\mu}\overline{\left[\boldsymbol{\nabla}\times(\mathbf{u}'_{\mathbf{s}} + \mathbf{u}'_{\mathbf{c}})\right]^2} = \frac{1}{2}\bar{\mu}\overline{(\boldsymbol{\nabla}\times\mathbf{u}'_{\mathbf{s}})^2},$$
$$\varepsilon_{\mathrm{II}} = -\frac{2}{3}\overline{\mu}\overline{\left(\frac{\partial u'_{c,i}}{\partial x_i}\right)\left(\frac{\partial u'_{c,k}}{\partial x_k}\right)}. \tag{A6}$$

It can be seen that ε_{I} and $\varepsilon_{\mathrm{II}}$ in Eq. (6) are only associated with u_s and u_c respectively, which means that ε_{I} and $\varepsilon_{\mathrm{II}}$ are actually the solenoidal part and the dilatational part of dissipation rate within the framework of the Helmholtz decomposition. Thus, our method in Sec. III A is equivalent to the Helmholtz decomposition.

APPENDIX B: GRID RESOLUTIONS OF ALL CASES

In Table II, we show the grid resolutions in wall units at both walls and at the center of the channel for cases TR3, TR1.9, TR1.4, and TR1.

TABLE III. The upper bound of the ζ^+ and ζ^* for the log layer, with the lower bound of the log layer being $\zeta^* = 30$.

Cases		$\zeta^+_{\max}$ (upper bound of ζ^+)	$\zeta^*_{\max}$ (upper bound of ζ^*)
TR3	hot wall	41.04	105.87
	cold wall	206.91	551.63
TR1.9	hot wall	86.79	104.87
	cold wall	207.73	454.31
TR1.4	hot wall	348.19	205.79
	cold wall	181.35	308.78
TR1		211.20	252.64

APPENDIX C: RANGE OF ζ FOR THE LOG LAYER

In Table III, we show the range of ζ for the log layer in cases TR3, TR1.9, TR1.4, and TR1.

[1] G. Simeoni, T. Bryk, F. Gorelli, M. Krisch, G. Ruocco, M. Santoro, and T. Scopigno, The Widom line as the crossover between liquid-like and gas-like behaviour in supercritical fluids, Nat. Phys. **6**, 503 (2010).

[2] D. Bolmatov, V. Brazhkin, and K. Trachenko, Thermodynamic behavior of supercritical matter, Nat. Commun. **4**, 2331 (2013).

[3] L. Xu, P. Kumar, S. Buildyrev, S. Chen, P. Poole, F. Sciortino, and H. Stanley, Relation between the Widom line and the dynamic crossover in systems with a liquid–liquid phase transition, Proc. Natl. Acad. Sci. USA **102**, 16558 (2005).

[4] H. Nemati, A. Patel, B. Boersma, and R. Pecnik, The effect of thermal boundary conditions on forced convection heat transfer to fluids at supercritical pressure, J. Fluid Mech. **800**, 531 (2016).

[5] J. W. R. Peeters, R. Pecnik, M. Rohde, T. H. J. J. van der Hagen, and B. J. Boersma, Turbulence attenuation in simultaneously heated and cooled annular flows at supercritical pressure, J. Fluid Mech. **799**, 505 (2016).

[6] K. Kim, J. P. Hickey, and C. Scalo, Pseudophase change effects in turbulent channel flow under transcritical temperature conditions, J. Fluid Mech. **871**, 52 (2019).

[7] M. X. Yao, Z. Sun, C. Scalo, and J. P. Hickey, Vortical and thermal interfacial layers in wall-bounded turbulent flows under transcritical conditions, Phys. Rev. Fluids **4**, 084604 (2019).

[8] J. H. Bae, J. Y. Yoo, and H. Choi, Direct numerical simulation of turbulent supercritical flows with heat transfer, Phys. Fluids **17**, 105104 (2005).

[9] P. Bradshaw, The effect of mean compression or dilatation on the turbulence structure of supersonic boundary layers, J. Fluid Mech. **63**, 449 (1974).

[10] J. W. R. Peeters, R. Pecnik, M. Rohde, T. H. J. J. van der Hagen, and B. J. Boersma, Characteristics of turbulent heat transfer in an annulus at supercritical pressure, Phys. Rev. Fluids **2**, 024602 (2017).

[11] F. Li, B. Pei, and B. Bai, Scaling laws of statistics of wall-bounded turbulence at supercritical pressure: Evaluation and mechanism, Phys. Fluids **34**, 085104 (2022).

[12] P. C. Ma, X. I. A. Yang, and M. Ihme, Structure of wall-bounded flows at transcritical conditions, Phys. Rev. Fluids **3**, 034609 (2018).

[13] S. Kawai, Heated transcritical and unheated non-transcritical turbulent boundary layers at supercritical pressures, J. Fluid Mech. **865**, 563 (2019).

[14] N. Mansour, J. Kim, and P. Moin, Reynolds-stress and dissipation-rate budgets in a turbulent channel flow, J. Fluid Mech. **194**, 15 (1988).

[15] C. Speziale and T. Gatski, Analysis and modelling of anisotropies in the dissipation rate of turbulence, J. Fluid Mech. **344**, 155 (1997).

[16] S. Pirozzoli, Revisiting the mixing-length hypothesis in the outer part of turbulent wall layers: Mean flow and wall friction, J. Fluid Mech. **745**, 378 (2014).
[17] Y. Y. Bae, E. S. Kim, and M. H. Kim, Application of compressible Reynolds-averaged governing equations to turbulent mixed convection in supercritical fluids in heated vertical tubes, Int. J. Heat Fluid Flow **76**, 85 (2019).
[18] A. Patel, J. W. R. Peeters, B. J. Boersma, and R. Pecnik, Semi-local scaling and turbulence modulation in variable property turbulent channel flows, Phys. Fluids **27**, 095101 (2015).
[19] A. Patel, B. J. Boersma, and R. Pecnik, Scalar statistics in variable property turbulent channel flows, Phys. Rev. Fluids **2**, 084604 (2019).
[20] M. C. Drake, R. W. Pitz, and W. Shyy, Conserved scalar probability density functions in a turbulent jet diffusion flame, J. Fluid Mech. **171**, 27 (1986).
[21] M. Ferchichi and S. Tavoularis, Scalar probability density function and fine structure in uniformly sheared turbulence, J. Fluid Mech. **461**, 155 (2002).
[22] J. Guo, X. I. A. Yang, and M. Ihme, Structure of the thermal boundary layer in turbulent channel flows at transcritical conditions, J. Fluid Mech. **934**, A45 (2022).
[23] T. H. Chung, M. Ajlan, L. L. Lee, and K. E. Starling, Generalized multiparameter correlation for nonpolar and polar fluid transport properties, Ind. Eng. Chem. Fund. **27**, 671 (1988).
[24] A. Congiunti, C. Bruno, and E. Giacomazzi, Supercritical combustion properties, in *41st Aerospace Sciences Meeting and Exhibit* (AIAA, Reno, NV, 2003), p. 478.
[25] J. P. Hickey, P. C. Ma, M. Ihme, and S. Thakur, Large eddy simulation of shear coaxial rocket injector: Real-fluid effects, in *49th AIAA/ASME/SAE/ASEE Joint Propulsion Conference* (AIAA, Reston, VA, 2013), p. 4071.
[26] P. G. Huang, G. N. Coleman, and P. Bradshaw, Compressible turbulent channel flows: DNS results and modeling, J. Fluid Mech **305**, 185 (1995).
[27] A. V. Johansson, P. H. Alfredsson, and J. Kim, Evolution and dynamics of shear-layer structures in near-wall turbulence, J. Fluid Mech. **224**, 579 (1991).
[28] J. Jiménez, The autonomous cycle of near-wall turbulence, J. Fluid Mech. **389**, 335 (1999).
[29] A. Patel, B. J. Boersma, and R. Pecnik, The influence of near-wall density and viscosity gradients on turbulence in channel flows, J. Fluid. Mech. **809**, 793 (2016).
[30] Y. Morinishi, S. Tamano, and K. Nakabayashi, Direct numerical simulation of compressible turbulent channel flow between adiabatic and isothermal walls, J. Fluid Mech. **502**, 273 (2004).
[31] J. R. Baltzer and D. Livescu, Variable-density effects in incompressible non-buoyant shear-driven turbulent mixing layers, J. Fluid Mech. **900**, A16 (2020).
[32] J. Lee, S. Y. Jung, H. J. Sung, and T. A. Zaki, Effect of wall heating on turbulent boundary layers with temperature-dependent viscosity, J. Fluid Mech. **726**, 196 (2013).
[33] F. Zonta, C. Marchioli, and A. Soldati, Modulation of turbulence in forced convection by temperature-dependent viscosity, J. Fluid Mech. **697**, 150 (2012).
[34] Y. S. Zhang, W. T. Bi, F. Hussain, X. L. Li, and Z. S. She, Mach-Number-Invariant Mean-Velocity Profile of Compressible Turbulent Boundary Layers, Phys. Rev. Lett. **109**, 054502 (2012).
[35] T. Y. Bai, K. P. Griffin, and L. Fu, Compressible velocity transformations for various noncanonical wall-bounded turbulent flows, AIAA J. **60**, 4325 (2022).
[36] S. Jagannathan and D. A. Donzis, Reynolds and Mach number scaling in solenoidally-forced compressible turbulence using high-resolution direct numerical simulations, J. Fluid Mech. **789**, 669 (2016).
[37] S. Sarkar, G. Erlebacher, M. Y. Hussaini, and H. O. Kreiss, The analysis and modelling of dilatational terms in compressible turbulence, J. Fluid Mech. **227**, 473 (1991).